CORONAVIRUS

Structure and inhibition of SARS-CoV-2 spike refolding in membranes

Michael W. Grunst¹*, Zhuan Qin¹†, Esteban Dodero-Rojas²†, Shilei Ding³, Jérémie Prévost^{3,4}, Yaozong Chen⁵, Yanping Hu⁶, Marzena Pazgier⁵, Shenping Wu⁷, Xuping Xie⁶, Andrés Finzi^{3,4}, José N. Onuchic^{2,8,9,10}, Paul C. Whitford^{11,12}*, Walther Mothes¹*, Wenwei Li¹*

The severe acute respiratory syndrome coronavirus 2 (SARS-CoV-2) spike protein binds the receptor angiotensin converting enzyme 2 (ACE2) and drives virus-host membrane fusion through refolding of its S2 domain. Whereas the S1 domain contains high sequence variability, the S2 domain is conserved and is a promising pan-betacoronavirus vaccine target. We applied cryo-electron tomography to capture intermediates of S2 refolding and understand inhibition by antibodies to the S2 stem-helix. Subtomogram averaging revealed ACE2 dimers cross-linking spikes before transitioning into S2 intermediates, which were captured at various stages of refolding. Pan-betacoronavirus neutralizing antibodies targeting the S2 stem-helix bound to and inhibited refolding of spike prehairpin intermediates. Combined with molecular dynamics simulations, these structures elucidate the process of SARS-CoV-2 entry and reveal how pan-betacoronavirus S2-targeting antibodies neutralize infectivity by arresting prehairpin intermediates.

evere acute respiratory syndrome coronavirus 2 (SARS-CoV-2) is the causative agent for COVID-19 and remains a global public health threat. The SARS-CoV-2 spike glycoprotein mediates entry into host cells by recognition of the cellular receptor angiotensin converting enzyme 2 (ACE2). Spike is a trimer of heterodimers composed of S1 and S2 subunits, which are cleaved by the host protease, furin, into a metastable state held together by noncovalent bonds (1). Spike activation for fusion is initiated by the S1 receptor binding domain (RBD) engaging host receptor ACE2, which triggers conformational changes in spike that promote shedding of the S1 domain (2). The exposed S2 domain is then thought to extend and insert the fusion peptide (FP) into the host membrane to bridge the virus and host membranes and form the "prehairpin intermediate" structure (1-7). This prehairpin intermediate structure is believed to be short-lived and to fold back onto itself through hydrophobic interactions of the heptad

¹Department of Microbial Pathogenesis, Yale University, New Haven, CT, USA, ²Center for Theoretical Biological Physics. Rice University, Houston, TX, USA. ³Centre de Recherche du CHUM, Montréal, QC H2X OA9, Canada. ⁴Département de Microbiologie, Infectiologie et Immunologie, Université de Montréal, Montréal, QC H3T 1J4, Canada. 5Infectious Disease Division, Department of Medicine, Uniformed Services University of the Health Sciences, Bethesda, MD 20814-4712, USA. ⁶Department of Biochemistry and Molecular Biology, University of Texas Medical Branch, Galveston, TX 77555, USA. ⁷Department of Pharmacology, Yale University, West Haven, CT 06516, USA. 8Department of Physics and Astronomy, Rice University, Houston, TX, USA. 9Department of Chemistry, Rice University, Houston, TX, USA. ¹⁰Department of Biosciences, Rice University, Houston, TX, USA. 11 Center for Theoretical Biological Physics, Northeastern University, Boston, MA, USA. 12 Department of Physics, Northeastern University, Boston, MA, USA.

*Corresponding author. Email: wenwei.li@yale.edu (W.L.); walther.mothes@yale.edu (W.M.); mikey.grunst@yale.edu (M.W.G.); p.whitford@northeastern.edu (P.C.W.)

†These authors contributed equally to this work.

repeat 1 (HR1) and HR2 domains (3, 7). Backfolding or "zippering" of S2 initiates fusion of the virus and host membranes (3, 8), followed by the transition of S2 into the postfusion conformation as a six-helix bundle with a rodlike shape (9–11).

Most neutralizing antibodies generated in response to SARS-CoV-2 infection or spike immunogens target the spike S1 subunit, which consists of the RBD and the N-terminal domain (NTD). Antibodies that target the RBD of S1 can neutralize SARS-CoV-2 by precluding RBD binding to ACE2 (either through direct competition or steric hindrance), locking RBD in a "down" conformation, or causing S1 to shed and prematurely triggering spikes to the postfusion state (12-18). SARS-CoV-2 variants of concern (VOCs) have rapidly acquired mutations in the S1 domain to escape neutralization by convalescent sera, vaccine sera, and monoclonal antibodies (19-25). Conversely, the spike S2 domain, particularly the stem-helix region, is highly conserved among betacoronaviruses (26, 27). Antibodies and inhibitors that target the stem-helix have high cross-reactivity against betacoronaviruses, including SARS-CoV-2 VOCs, SARS-CoV, and Middle East respiratory syndrome coronavirus (MERS-CoV) (14, 26-33). S2 can also be immunogenic and elicit broadly reactive vaccine or convalescent sera (34-36). Further, S2-based subunit vaccines were shown to be protective against SARS-CoV-2 challenge in mice, Syrian golden hamsters, and rhesus macagues (37, 38).

Although the purified spike has been structurally well characterized in complex with soluble ACE2 in vitro, it remains unclear how spike trimers engage ACE2 dimers within membranes and undergo refolding into the postfusion conformation. There is growing interest in the development of antibodies and immu-

nogens targeting the S2 subunit; however exact mechanism by which these antibo inhibit the refolding of spike from the prefusion to the postfusion state is still unclear. Defining the inhibitory mechanism of antibodies to S2 is critical for rational S2-based immunogen and monoclonal antibody design against known and emerging coronaviruses.

Spike-receptor complexes and fusion intermediates captured at membrane-membrane interfaces

To better understand the spike-mediated fusion process, we developed a system to observe early virus entry and fusion events by using cryoelectron tomography (crvo-ET) and subtomogram averaging. We generated virus-like particles (VLPs) with distinct retroviral cores from human immunodeficiency virus (HIV-1) and murine leukemia virus (MLV) decorated with either spike or ACE2, respectively (spike_{VLP} and ACE2_{VI P}) (Fig. 1A). The advantages of this system include achieving high production of spike- and ACE2-bearing particles compared with use of coronavirus-like particles or extracellular vesicles (3, 14, 17), avoiding the need for chemical fixation and reducing heterogeneity in particle size and morphology. Thus, it allows us to capture spike-ACE2 membrane interfaces after co-incubation at high frequency and uniformity for imaging and subtomogram averaging of membrane-bound spike structures.

We confirmed the fusogenicity of spike- and ACE2-decorated VLPs using a split nano luciferase complementation-based virus-cell fusion assay. Spike_{VLP}s fused with cells expressing ACE2 in a temperature-dependent and spikedependent manner (Fig. 1B). Likewise, ACE2_{VLP}s fused with spike-expressing cells in a temperature and ACE2-dependent manner (Fig. 1B). Spike- and ACE2-decorated VLP mixtures were incubated at 4° or 37°C and imaged by using the Titan Krios cryo-electron microscope. Interactions between VLPs with HIV-1 and MLV capsid cores were readily identified owing to the distinct capsid morphology (Fig. 1, A and C). VLP interfaces derived from 4°C incubation contained intact prefusion spikes that were cross-linked by ACE2 dimers (Fig. 1D and fig. S1). Transitioning from 4° to 37°C, spike-ACE2 complexes largely disappeared, and rodlike structures appeared that bridged membrane-membrane interfaces (Fig. 1E and fig. S2A). Point-like protrusions and distortions on $ACE2_{VLP}$ membrane were observed at the tip of the rods, indicating that a pulling force was being exerted by these structures (fig. S2A). Both structures were also observed at 4° and 37°C, respectively, between VLPs and membrane blebs (fig. S3, A and B). Membrane blebs were more heterogeneous in size and morphology, which prompted the use of VLPs in subsequent analyses. Together, the VLP system

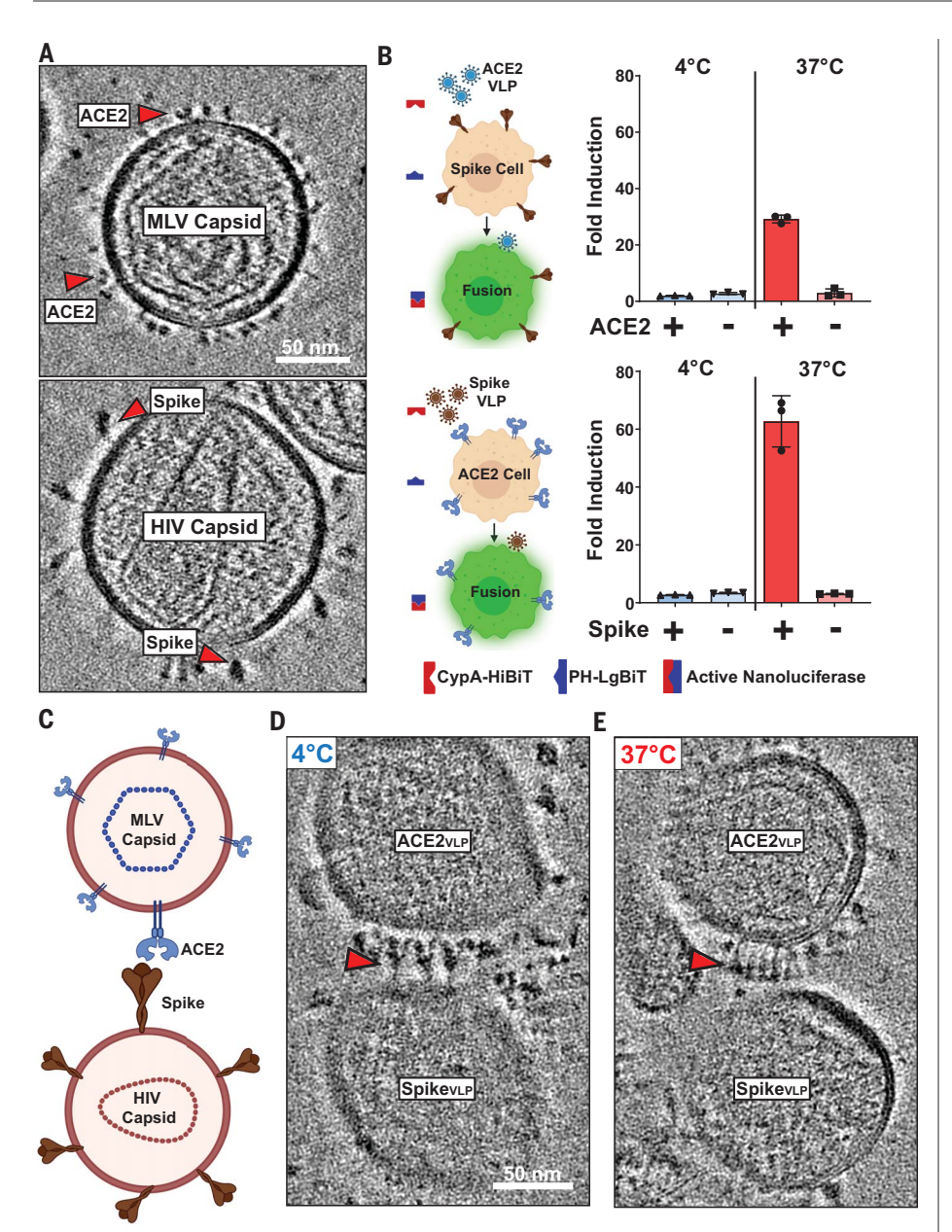


Fig. 1. SARS-CoV-2 spike-ACE2 complexes and fusion intermediates captured at membrane-membrane interfaces. (**A**) Representative tomographic slices of (top) MLV particles decorated with ACE2 and (bottom) HIV particles decorated with spike. (**B**) (Left) Cartoon representation of VLP-to-cell fusion nanoluciferase complementation assay. (Right) Spike-decorated (spike+), ACE2-decorated (ACE2+), or bald VLPs (–) containing CypA-HiBiT were incubated with endurazine-labeled target cells expressing (top) spike or (bottom) ACE2 and membrane-bound PH-LgBiT at 4° and 37°C for 1 hour before assessment of NanoLuc (Promega) activity. Error bars indicate the standard deviation from triplicate infections. Data shown are representative from two independent experiments. (**C**) Cartoon representation of interacting (bottom) spike_{VLP}s and (top) ACE2_{VLP}s. (**D** and **E**) Representative tomographic slices of spike- and ACE2-decorated VLPs co-incubated at (D) 4°C or (E) 37°C. Red arrowheads indicate spikes at the membrane-membrane interfaces.

provides experimental access to spike attachment and activation.

Spikes are cross-linked by ACE2 dimers in membranes

We next structurally characterized the attachment of spike to ACE2 in membranes. To facil-

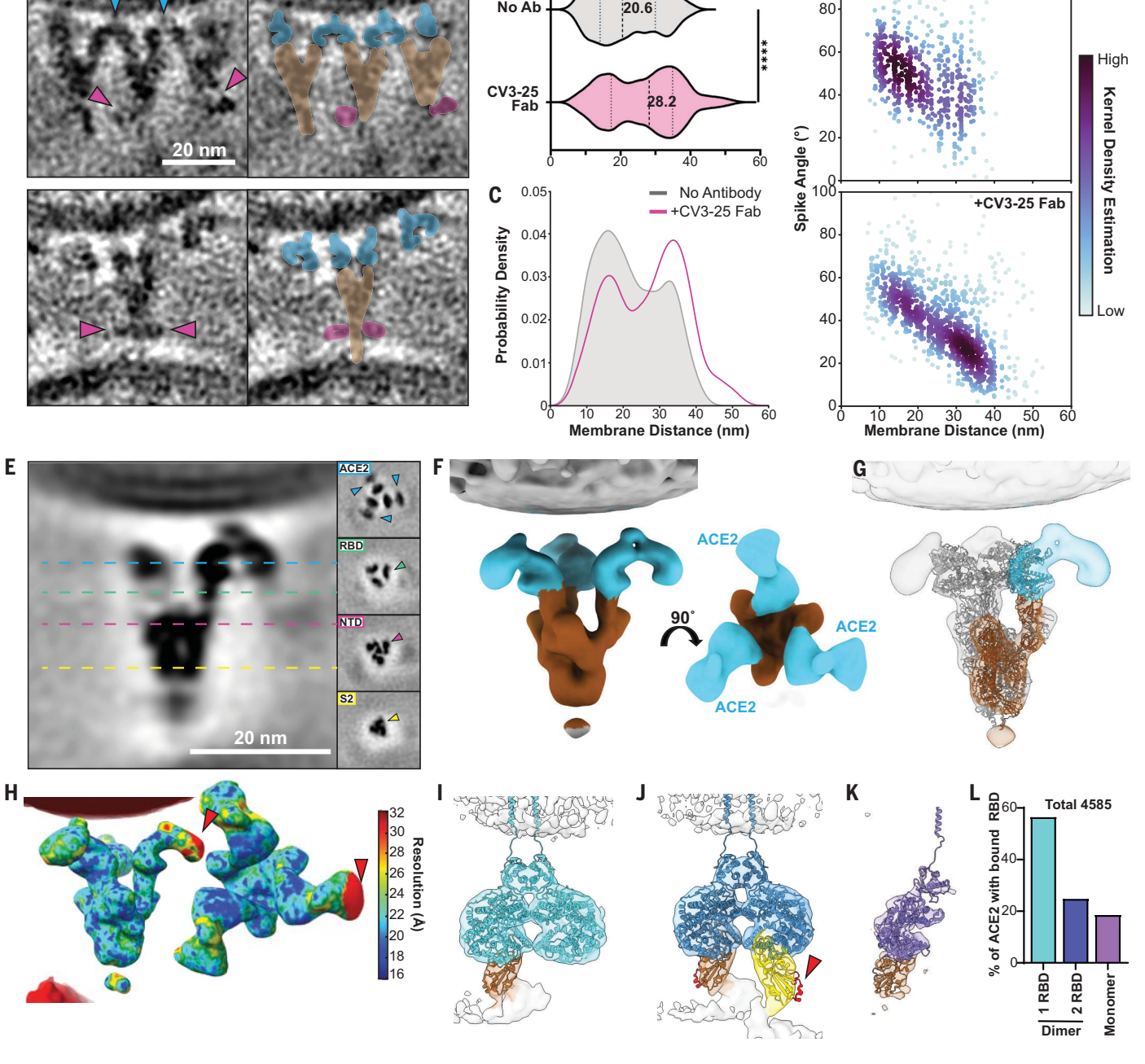
itate structure determination, we introduced CV3-25 Fab, an antibody targeting the stem-helix (14, 27, 39, 40), to the spike- and ACE2-bearing VLP mixture incubated at 4°C. CV3-25 was previously shown to reduce spike tilting (14). One or multiple CV3-25 Fabs were observed to bind to the spike-ACE2 complex at the stem-

helix region, which is consistent with previous results of CV3-25 binding to spikes alone (Fig. 2A) (14). The presence of CV3-25 Fab was associated with an ~8-nm increase in the median distance. which is defined by two points located at the nearest approach between the spike_{VLP} and ACE2_{VLP} interface membranes (Fig. 2B and table S1). The distributions of spike_{VLP}-ACE2_{VLP} membrane-membrane distances suggested two apparent modes at 16 to 17 nm and 33 to 34 nm distance both with and without CV3-25 Fab (Fig. 2C and fig. S4, A and C). CV3-25 Fab was associated with a strong shift in the distribution toward the second mode (Fig. 2C and fig. S4, A and C). Additionally, strong associations between the spike tilt angles and the membranemembrane distances were observed in both the presence and absence of CV3-25 Fab (Fig. 2D and fig. S5A). These data indicate that CV3-25 Fab reduces spike tilting in the spike-ACE2 complex, preventing spike_{VLP} and ACE2_{VLP} membranes from approaching. Reduced spike tilting facilitated structural characterization of the spike-ACE2 complex at membrane-membrane interfaces.

We performed subtomogram averaging of the prefusion spike-ACE2 complexes in the presence and absence of CV3-25 Fab. The combined averaged structure of the prefusion spike-ACE2 complexes derived from ~2000 subtomograms revealed spike in a three-RBD-up conformation, with each RBD occupied by one ACE2 dimer (Fig. 2, E and F, and fig. S6). Classification did not reveal spikes with only one or two RBDs bound by ACE2. All spike trimers appeared bound to three ACE2 molecules (EMD-42857) (Fig. 2F). An atomic model of spike bound with three monomeric ACE2s [Protein Data Bank (PDB) ID 7EDJ] fit well into the cryo-ET density map (Fig. 2G), indicating that the interaction between spike trimers and ACE2 dimers in membranes was established by the similar RBD-ACE2 interaction observed with soluble proteins (41).

The local resolution analysis of the prefusion spike-ACE2 averaged structure indicated lower resolutions of ACE2 dimers compared with spike trimers, especially at the outer halves of ACE2 dimers (Fig. 2H). This suggests heterogeneity among ACE2 dimers within these complexes. We therefore performed subtomogram averaging and classification of ACE2 molecules in complex with RBDs. Classification revealed the presence of ACE2 dimers bound to one RBD, ACE2 dimers bound to two RBDs, and ACE2 monomers bound to one RBD (EMD-42875, EMD-42876, and EMD-42877) (Fig. 2, I to K). The structure of an ACE2 dimer bound to two RBDs is reflected in the observed cross-linking of spikes in tomographic slices, where one ACE2 dimer can bind two RBDs from neighboring spikes (Fig. 1D and fig. S1). ACE2 dimers binding two RBDs from the same spike were not observed. An atomic model with

CV3-25 Fab



В

No Ab

Fig. 2. Spikes are cross-linked by ACE2 dimers in membranes. (A) Representative tomographic slices of spike- and ACE2-decorated VLPs co-incubated at 4°C in the presence of CV3-25 Fab. (Top) One or (bottom) multiple CV3-25 Fabs can be seen binding to the spike stem-helix. Magenta arrows indicate CV3-25 Fab, and blue arrows indicate ACE2 cross-linking spikes. Colored annotations are shown at right (blue, ACE2; brown, spike; magenta, CV3-25). (B) The distances between interacting spike- and ACE2-VLP membranes in the presence (n = 302 interfaces) and absence (n = 93 interfaces) of CV3-25 Fab were compared by using a Mann-Whitney U test (****P < 0.0001). (**C**) The distributions of membrane distance values in the presence and absence of CV3-25 Fab are compared. (D) Tilt angles of spike-ACE2 complexes on virion surfaces were plotted against their respective spike_{VLP}-ACE2_{VLP} membrane distances. The color mapping indicates the point density determined through kernel density estimation. No Antibody, 93 distinct membrane distances and 683 spike angles; +CV3-25 Fab, 302 distinct membrane distances and 1269 spike angles. (E) Spike-ACE2 complexes were aligned through subtomogram averaging

(EMD-42857). The image shows a central slice through the averaged EM density. Images at right correspond to dashed lines that indicate top-view slices along the length of the spike. (F and G) Isosurface representations of (F) the spike-ACE2 complex with (G) the fitted atomic model of spike binding to soluble ACE2 [PDB 7EDJ (41)]. Brown, spike; blue, ACE2. (H) Local-resolution estimation of the spike-ACE2 structure is shown. The red arrowheads indicate lower-resolution areas in ACE2. (I to K) Isosurface representations of three classes of ACE2 molecules determined by means of subtomogram averaging and classification focusing on ACE2-RBD interface within spike-ACE2 complexes. (I) One-RBD-bound ACE2 dimer (EMD-42875). (J) Two-RBD-bound ACE2 dimer (EMD-42876). (K) RBD-bound ACE2 monomer (EMD-42877). PDB 6M17 was fit into the EM density maps (42). In (J), the second RBD from a different cross-linked spike is shown in yellow. The red arrowhead indicates imperfect agreement (red coloring) between the EM map and atomic model. (L) The relative class percentages of ACE2 bound with RBD are shown.

D

No Antibody

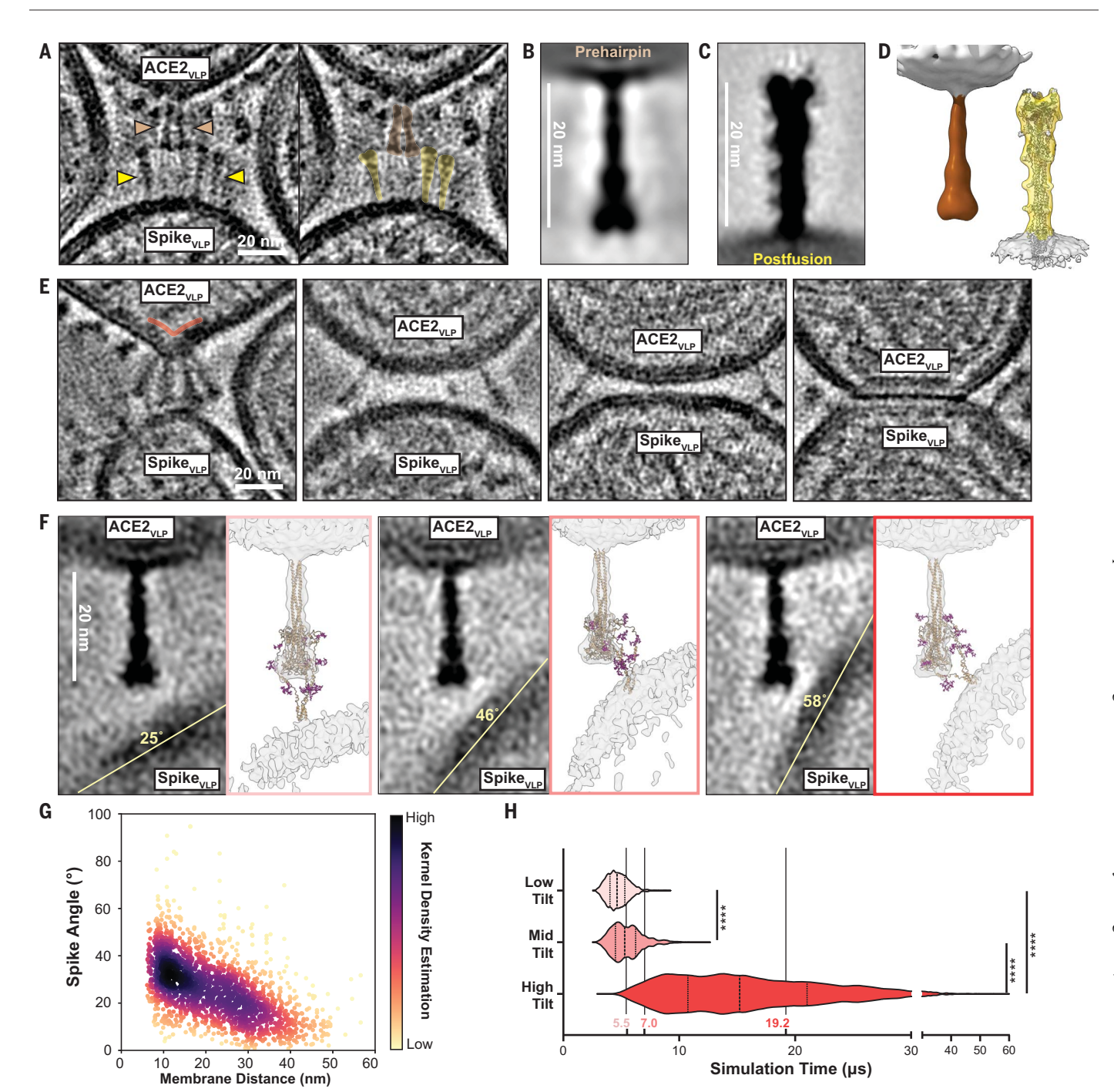


Fig. 3. Spikes transition to prehairpin intermediates after temperature activation. (A) A representative tomographic slice of spike- and ACE2-decorated VLPs co-incubated at 37°C. Prehairpin intermediates (brown) are distinguished from postfusion structures (yellow) by their opposite topology. (B and C) Central slices of EM density maps obtained from subtomogram averaging of (B) spike prehairpin intermediates (EMD-42859) and (C) postfusion spikes (EMD-42865). (D) Isosurface representations of the (left) prehairpin intermediate and (right) postfusion spike. PDB 8FDW was fit into the postfusion density map (11). (E) Representative tomographic slices of prehairpin intermediates observed at various stages of S2 refolding. (Left) Extended intermediates. Red annotation indicates membrane protrusion. (Left middle and right middle) Partial backfolding. (Right) Contracting membranes. (F) Classification of the prehairpin intermediates revealed distinct classes with spike_{VLP} membranes present at different angles relative to ACE2_{VLP} membranes (yellow line). Central slices through the EM density

maps (left) along with the isosurface views (right) are shown. Models from all-atom MD simulations of spike refolding were selected on the basis of their agreement with EM density maps. Residues 706 to 814 and 919 to 1234 of the spike protein and glycans associated with ${\rm Asn^{1158}}$, ${\rm Asn^{1173}}$, and ${\rm Asn^{1194}}$ are shown (magenta). (**G**) Tilt angles of prehairpin intermediates on virion surfaces were plotted against their respective spike_VLP-ACE2_VLP membrane distances. The color mapping indicates the point density determined through kernel density estimation. The scatter plot contains 909 distinct membrane distances corresponding to 2095 individual spike angles. (**H**) The distributions of simulated ensembles, that agree with prehairpin intermediate EM density maps, throughout the time course of MD simulations. The time points of the models fitted in the EM density maps (F) are labeled. Distributions were compared by using a Kruskal Wallis test with Dunn's multiple comparisons test (****P < 0.0001). Low tilt, n=10,732 structures; medium tilt, n=13,002 structures; high tilt, n=121,139 structures.

an ACE2 dimer bound to soluble RBDs (PDB ID 6M17) agreed well with the electron microscopy (EM) density maps of one-RBD-bound ACE2 dimers and ACE2 monomers (Fig. 2, I and K) (42). However, the RBDs in the atomic model had imperfect agreement with the two-RBDbound ACE2 density map and appeared rotated slightly outward from the EM density (Fig. 2J, red arrow). This suggests that there may be additional conformational changes in spike to facilitate ACE2 cross-linking that were not previously captured in single-particle cryo-EM structures (42). The relative percentages of ACE2 molecules bound to RBDs revealed that ~85% of RBD-associated ACE2 molecules were dimerized, and about one-fourth of ACE2 dimers were bound to two RBDs (Fig. 2L). The tilting of ACE2 dimer on the membrane may also facilitate its binding to one or two spike RBDs (fig. S5, B to D), which is consistent with previous prediction from molecular dynamics (MD) simulations (43). From the spike perspective, only spike trimers binding three ACE2 molecules resulting in all three RBDs oriented up were observed. Collectively, these data offer structural evidence that spike trimers and ACE2 dimers are mutually cross-linked at membrane interfaces.

Spikes transition to prehairpin intermediates at increased temperature

Unlike 4°C co-incubation of spike_{VLP}s and ACE2_{VLP}s, which generated prefusion spike-ACE2 complexes, incubation at 37°C resulted in the appearance of spike S2 fusion intermediates (Fig. 1E and fig. S2A). Additionally, shed S1 subunits were found to coat ACE2 dimers on MLV_{ACE2} VLPs (fig. S2B). S2 fusion intermediates could be easily distinguished from postfusion structures by the reversed topology, with the thicker head oriented toward the spike_{VLP} membrane and the rod anchored in the $ACE2_{VLP}$ membrane (Fig. 3A). We performed subtomogram averaging of ~2000 fusion intermediate spikes derived from 275 tomograms (EMD-42859) (Fig. 3B). The HR2 regions and the spike_{VLP} membrane were unresolved, which reflects the heterogeneity of this region as suggested by previous studies (3, 7, 44). The distance from the HR1 ACE2_{VLP} membrane contact point and the head group is measured to be 21 nm, which is also consistent with previous observations in raw tomographic data and MD simulations (3, 7). Subtomogram averaging was additionally performed for ~6500 postfusion spikes present in these tomograms (EMD-42865) (Fig. 3C). The postfusion spike structure shows the presence of extra density along the rod body, which is consistent with postfusion spike atomic models (Fig. 3, C and D), suggesting that the HR2 domains are repositioned near the exposed HR1 domain after spike refolding (11, 45-48).

The tomograms revealed spike fusion intermediates captured at various stages of refolding, from extended intermediates, to partial backfolding, to contacting spike and ACE2 membranes (Fig. 3E). Therefore, we performed classification on the averaged fusion intermediate structure. Whereas the $spike_{VLP}$ membrane is absent in the combined average (Fig. 3B), the spike_{VLP} membrane appeared in class averages with increasing membrane tilt angle relative to the ACE2_{VLP} target membrane (Fig. 3F, left). Further classification revealed more structures with different tilting of the spike membrane relative to the ACE2 membrane (fig. S7). These results suggest that the position of the spike_{VLP} membrane relative to the $ACE2_{VLP}$ membrane is dynamic and that fusion intermediates were captured during the S2 refolding process when membranes move progressively closer together. We additionally found a strong relationship between the prehairpin intermediate spike angle and the distance between the spike_{VLP} and ACE2_{VLP} membranes (Fig. 3G and fig. S5E). A closer analysis of the distribution of membrane distances suggested the presence of a major mode near 11 nm (membranes in close proximity) and other notable modes near 16, 23, and 30 nm (fig. S4, B and C). Collectively, this analysis displays a continuum of increasing spike angles corresponding to decreasing membrane distances, along with intermediates exhibiting increased occupancy.

We noticed that the EM density maps of the S2 fusion intermediates are very similar to conformations that were predicted with recent simulations of the prefusion-to-postfusion transition of the spike protein (7). In that study, a total of 1000 transitions between pre- and postfusion conformations were simulated by using an all-atom model with structure-based energetics ("SMOG" model) (49). These simulations were found to sample configurations that are compatible with the cryo-ET class averages described here (table S2). By comparing the MD simulations of the spike transition with the cryo-ET subclass averages, we identified ensembles of structures that agree with the EM density maps (Fig. 3F). These structural ensembles reflect early, intermediate, and late time points in the simulations (Fig. 3H), Because the simulation lacks a target membrane, the placement of the FP regions was not previously determined. However, the strong rod-like EM density that is a hallmark of all subclass averages indicates that the prehairpin HR1 with the N-terminal FPs likely adopts a conformation similar to that of the postfusion spike in the target membrane very early (fig. S8) (11). Together, subtomogram averaging and classification reveal different conformations of the spike prehairpin intermediate progressing along increasing membrane tilt angles that is the consequence of S2 refolding driving the membranes closer together (movie S1).

Broadly neutralizing antibodies to stem-helix inhibit spike refolding

Antibodies targeting the conserved spike S2 domain are of considerable interest for addressing emerging VOCs and for potential broad-spectrum activity against betacoronaviruses (14, 26, 27, 30, 31, 33, 34). Because of the low variation in the epitopes, antibodies targeting the S2 stem-helix neutralize SARS-CoV and all SARS-CoV-2 variants, from the original strain at the beginning of the pandemic to recent variants such as BA.2.86 and EG.5.1 (Fig. 4A and fig. S9, A and B). Within this group of antibodies, CV3-25 stands out because of its distinctive binding to the exposed face of the stem-helix. By contrast, the other stem-helix antibodies, such as CC25.106 and CC99.103, bind to the buried face, which is concealed within the three-helix bundle of prefusion spike (Fig. 4B). None of these antibodies bind to postfusion spike (14, 27, 50). It has been suggested through single-particle cryo-EM studies of prefusion spike that these antibodies bind to a disrupted three-helix bundle (51). Therefore, we hypothesized that they may bind to the spike prehairpin intermediate conformation after separation of the stem-helices.

To identify the stage at which antibody binding may occur during the spike refolding process, we assessed previous MD simulations of the prefusion-to-postfusion conformational transition (7). For those simulations, a structurebased SMOG model was applied (49), in which all interactions present in the postfusion conformation were explicitly defined to be stable. Interactions not found in the poststructure are purely based on excluded volume, ensuring that only sterically accessible conformations are sampled. To incorporate the effect of a viral membrane, the transmembrane domain (TM) region was restrained to a plane. Qualitatively, this model treats the prefusion conformation as an energetically loaded state, in which energy is released as the system approaches the postfusion conformation. Earlier simulations with this model ("Spike Force Field": supplementary materials) showed that molecular sterics strongly limits the possible interconversion pathways and that the glycans can strongly influence the kinetics (7). We analyzed the previous simulations and found that the CV3-25 and CC25.106 epitopes are transiently exposed, where the antibody-accessible surface area (AbASA) increases, before decreasing as the postfusion conformation is reached (Fig. 4C and fig. S10, A and B). Although the CV3-25 epitope seems to be more exposed in the postfusion conformation, the orientations of S2 residues suggest steric clashes that are incompatible with binding as defined

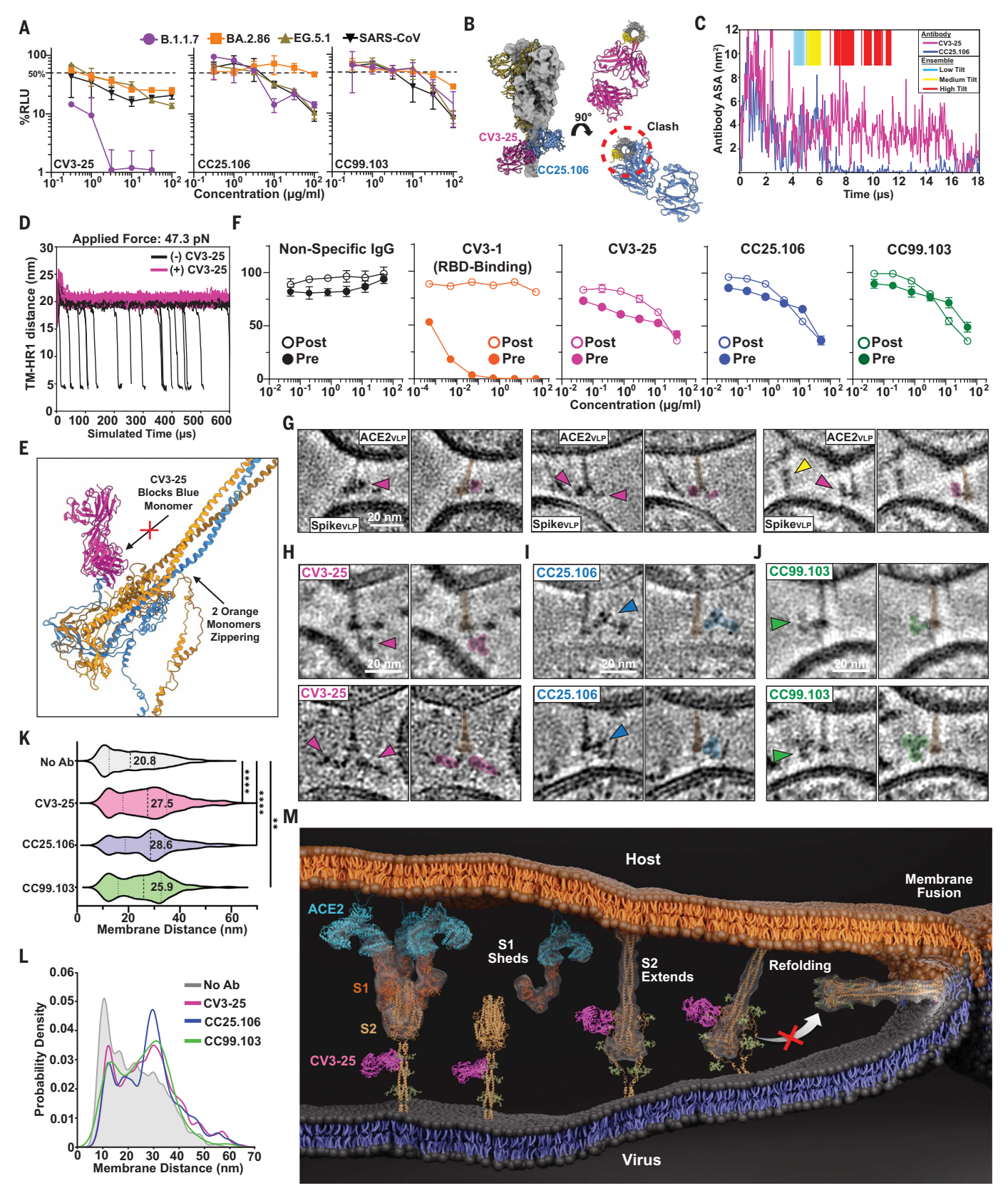


Fig. 4. Broadly neutralizing antibodies to stem-helix inhibit spike refolding. (A) Neutralization activities of stem-helix antibodies against VLPs bearing spikes from indicated betacoronaviruses. Infectivity [percent relative light units (RLUs)] is shown, and error bars indicate standard deviation from duplicate wells.

Results are representative of at least three independent experiments. (**B**) Models of CV3-25 [magenta; PDB 7NAB (14)] and CC25.106 [blue; PDB 8DGU (27)] bound to SARS-CoV-2 stem-helix peptide were superimposed on the prefusion spike [PDB 6XR8 joined to a model of the full-length S2 stem (7, 9)]. CC25.106

shows a clash in binding with the prefusion spike. (C) AbASA for CV3-25 epitope (magenta) and CC25.106 epitope (blue) along a simulated prefusion-topostfusion transition of the spike. (D) MD simulations of spike refolding in the presence and absence of CV3-25 Fab with an applied normal membrane force of 47.3 pN. The distances between the TM and the heptad region 1 (HR1) of the spike protein along simulated trajectories with and without CV3-25 were calculated (fig. S12). (E) A representative structural snapshot from the simulated trajectories in (D) is shown. CV3-25 (magenta) can halt the prefusion-topostfusion transition of the spike protein by blocking the HR2-HR1 zippering process of one of the monomers (blue). (F) Stem-helix antibodies and the RBDtargeting antibody CV3-1 were compared for their virus neutralization activity before and after attachment to target cells by using HIV-decorated spike virions with an HIV-integrated Gaussia luciferase reporter. Error bars indicate the standard deviation from triplicate wells, and results shown are representative of three independent experiments. (G) Spike_{VLP}s and ACE2_{VLP}s were coincubated at 37°C in the presence of CV3-25 Fab. Three representative tomographic slices are shown with magenta arrowheads indicating Fab (left), and brown and

magenta annotations corresponding to prehairpin intermediate spike and CV3-25 Fab, respectively (right). The yellow arrowhead indicates a postfusion spike. (**H** to **J**) Two representative tomographic slices of spike_{VI P}s and ACE2_{VI P}s co-incubated at 37°C in the presence of (H) CV3-25, (I) CC25.106, and (J) CC99.103. The antibodies are indicated by arrows (leftimages), and the prehairpin intermediate spikes (brown) and antibodies (magenta, blue, or green) are annotated (right images). Multiple IgG domains may be visible. (K) The distances between interacting spike- and ACE2-bearing membranes in the presence and absence of indicated antibodies were compared by using a Kruskal-Wallis test and Dunn's multiple comparisons test (****P < 0.0001, **P < 0.01). No Antibody (No Ab), n = 909 interfaces; CV3-25, n = 374 interfaces; CC25.106, n = 385 interfaces; CC99.103, n = 111 interfaces. (L) The distributions of membrane distance values in the presence and absence of indicated antibodies are compared. (M) A summary graphic of the structure and inhibition of spike refolding in membranes. The image was generated by using the simulated intermediate atomic models from Dodero-Rojas et al. and PDBs 6M17, 7EDJ, 7NAB, and 8FDW (7, 11, 14, 41, 42). The glossy encasing around atomic models indicates EM density from this study.

by the high-resolution structure of CV3-25 Fab in complex with S2 peptide (14). We next evaluated the distribution of AbASA values, calculated for the corresponding simulated ensemble for each cryo-ET density map of prehairpin intermediates (fig. S10C). Later-stage intermediates at higher tilt angles are associated with a decrease in AbASA for both CV3-25 and CC25.106 epitopes. Decreases in AbASA values are due to "zippering" of S2 at late time points during the conformational transition. which agrees with antibody-peptide structures and structures of prefusion and postfusion spikes (9, 11, 14, 27, 41). Glycans reduce the AbASA values (fig. S11), which is consistent with the notion of a glycan "shield" (52). However, disrupting the stem-helix glycan epitope only modestly increases CC25.106 and CC99.103 neutralization potency, indicating that fluctuations in glycan conformations transiently expose the stem-helix epitope to allow for antibody binding (27). Collectively, these data indicate that the epitopes for antibodies to S2 stem-helix are most exposed during early stages of S2 refolding.

To test the impact of CV3-25 binding on spike refolding, we modified the earlier theoretical model to include a single-bound CV3-25 molecule and the effect of the host membrane. In the current study, to mimic the presence of a host membrane, we introduced a constant force on the terminal region of HR1 that was directed normal to the viral membrane then performed our simulations with this extended model ("Spike+Host" and "Spike+Host+CV3-25" force fields; supplementary materials) to identify the influence of CV3-25 under different values of the force. Consistent with previous calculations (7), nearly every simulation reached the postfusion conformation in the absence of the applied force. However, this probability decreased when force was applied (fig. S12) and decreased more rapidly with force when CV3-25 was included in the simulations (Fig. 4D and fig. S12). When the antibody was present and the applied force was set to ~43.2 pN, the TM-HR1 distances plateaued at ~20 nm for almost every simulation. By contrast, when the antibody was absent, the majority of the simulations successfully reached the postfusion state. This difference is due to the antibody interfering with the HR1-HR2 zippering process (Fig. 4E), which reduces the force that spike may exert on the host membrane.

Antibodies to S2 stem-helix were also able to bind spike from SARS-CoV-2 variants and other betacoronaviruses on cell membranes in the absence and presence of soluble ACE2 (fig. S9C). We hypothesized that these antibodies could inhibit viral entry by precluding spike refolding after ACE2 binding when viruses attach to target cells. We therefore investigated inhibition of virus entry before or after the viruses attached to receptor-expressing cells. Whereas the RBD-targeting antibody CV3-1 could only inhibit virus entry before attachment, all S2 stem-helix antibodies inhibited virus entry both before and after attachment to a similar extent (Fig. 4F). These data suggest that antibodies targeting both the buried and exposed faces of the stem-helix can inhibit spike refolding after ACE2 binding.

We revisited the spike refolding by means of cryo-ET analysis at 37°C in the presence of antibodies targeting stem-helix. Samples were first prepared by using CV3-25 Fab domains for visualization (Fig. 4G and fig. S13), which showed the presence of CV3-25 Fab density near the head group of prehairpin intermediates at the approximate locations of the HR2 stem-helix (Fig. 4G and fig. S13). We next determined whether immunoglobulin G (IgG) binding to the exposed face (CV3-25) and the buried face (CC25.106 and CC99.103) would similarly bind to prehairpin intermediates. The Ig domains of all three antibodies were observed to bind near the head group of prehairpin intermediates (Fig. 4, H to J). All three antibodies resulted in greater distances between the $\mbox{spike}_{\mbox{\scriptsize VLP}}$ and $\mbox{ACE2}_{\mbox{\scriptsize VLP}}$ membranes (Fig. 4K and table S1). The presence of antibodies resulted in a strong shift in the distributions of membrane distances, with the highest density mode consistently near 30 nm (Fig. 4L and fig. S4, B and C). The mode near 30 nm was also detected in the absence of antibody, albeit much less prominent (fig. S4, B and C). Collectively, these data indicate that antibodies to stem-helix act by hindering the back-zippering of HR2 along the extended HR1 prehairpin, stabilizing a preexisting intermediate state and preventing the membranes from moving closer together (Fig. 4M and movie S2).

Structure and inhibition of spike on native SARS-CoV-2 virions

To ask whether the observations of spike proteins on spike_{VLPs} are reflective of what is observed with native SARS-CoV-2 virions, we used an attenuated strain of SARS-CoV-2 that lacked ORF3, -6, -7, and -8 ($\Delta 3678$), carrying green fluorescent protein (GFP) and bearing Omicron XBB.1.5 spike (XBB.1.5 $_{\Lambda 3678}$) (53). At 4°C, as we showed on spike_{VLP}s, we observed spike-ACE2 complexes between XBB.1.5 $_{\Delta 3678}$ and ACE2 $_{\rm VLP}$ membranes (fig. S14A-E), along with spike cross-linking by ACE2 dimers (fig. S14, C to E). At 37°C in the presence of antibody to S2 stemhelix, we observed prehairpin intermediate structures, such as those between spike_{VLP}s and ACE2_{VLP}s bound by antibody (fig. S14, F to J). Consistent with previous cryo-EM studies of the SARS-CoV-2 Delta strain, there were also interactions and prehairpin intermediates between XBB.1.5 $_{\Delta3678}$ virions (fig. S14J) (46). More XBB.1.5 $_{\Delta 3678}$ prefusion spike-ACE2 complexes were intact after 37°C incubation compared with those between spike_{VLP}s and ACE2_{VLP}s, where temperature activation had triggered nearly all of the prefusion spikes. Lesser XBB.1.5_{A3678} spike activation at 37°C suggests that SARS-CoV-2 virion fusion may require sequential activation processes such as S2' cleavage by host TMPRRS2 or endosomal cathepsin (54). These results with native

SARS-CoV-2 confirm ACE2-induced clustering of spikes and that antibodies to stem-helix can still recognize prehairpin intermediates of recently emerging variants.

Conclusions

The initial virus entry events mediated by SARS-CoV-2 spike, such as attachment to the ACE2 receptor, have been extensively investigated by using soluble components (42, 55-59). However, the interactions between spike and ACE2 in membranes that lead to S2-mediated membrane fusion are less well understood. We used a VLP-VLP system to increase the frequency of observed spike-ACE2 interfaces in membranes to enable subtomogram averaging. Subtomogram averaging permits a quantitative assessment of observed structural intermediates. Using this approach, we determined an averaged structure of spike-ACE2 prefusion complexes in membranes. Our findings suggest that the geometry of the RBD-ACE2 interaction prevents the binding of one ACE2 dimer to two RBDs on the same spike. Instead, it promotes ACE2 dimers to engage RBDs from neighboring spikes. These results reveal how ACE2 dimers cross-link spike trimers at membrane interfaces to facilitate spike clustering. ACE2-induced clustering of spike may point to additional advantages for adopting a dimeric cellular receptor for entry. In addition to ACE2 being used as a receptor for SARS-CoV-2, SARS-CoV, and human coronavirus NL63, MERS receptor DPP4 and human coronavirus 229E receptor APN are also dimeric (60-62).

Whereas VOCs have acquired constellations of mutations in the RBD and NTD of the S1 spike subunit, the S2 domain containing the fusion machinery remains highly conserved but it is structurally less understood. To study refolding of the S2 domain, we used temperature activation of membrane-bound prefusion spike-ACE2 complexes. Subtomogram averaging and classification revealed prehairpin intermediates in distinct stages of refolding, as suggested by the different relative spike_{VLP} and ACE2_{VLP} membrane angles. The ability of subtomogram averaging to reveal various prehairpin intermediates points to their existence as structural intermediates with a life span long enough that they can be captured and potentially targeted by antibodies or smallmolecule inhibitors.

The angles and distances between the spike HR2 and head-group domains of the averaged structures corresponded well with MD simulations of the spike prehairpin intermediate (7). With respect to the HR1-FP regions, their precise structural properties were previously not determined owing to the absence of a target membrane in the simulated model. However, the cryo-ET density maps suggest that the HR1-FP regions are bundled within the target membrane and more closely resemble

the postfusion conformation, as shown in recent cryo-EM structures of the postfusion spike in membranes (11). Our combination of cryo-ET and MD simulation arrives at a model for how S2 refolding drives the membranes together for fusion (movie S1).

Studying spike refolding in membranes provides a platform for investigating the inhibition of this process. Recently, an HR2-mimic lipopeptide fusion inhibitor was shown to enrich the S2 prehairpin intermediate at a late-stage conformation just before the final transition to the postfusion state (3). In this study, we have demonstrated that broadly reactive antibodies, targeting both the buried and exposed faces of the stem-helix, impede spike refolding by sterically blocking the back-zippering of HR2 onto the extended HR1 domains during the transition from prehairpin intermediate to the postfusion state (Fig. 4M and movie S2). This mechanism effectively arrests the fusion process at a preexisting intermediate. AbASA analysis of MD simulations indicates that the epitopes are exposed early during the refolding. The transient exposure of the buried S2 stem epitopes explains why these antibodies are relatively rare and exhibit reduced neutralizing potency as compared with that of RBD-targeting antibodies. Our structural work pinpointing the prehairpin intermediate as the main target of the antibodies to S2 stem-helix opens the door for immunogen design aimed at eliciting these antibodies more effectively.

REFERENCES AND NOTES

- 1. L. Duan et al., Front. Immunol. 11, 576622 (2020).
- A. J. Pak, A. Yu, Z. Ke, J. A. G. Briggs, G. A. Voth, Nat. Commun. 13, 1002 (2022)
- 3. T. C. Marcink et al., Sci. Adv. 8, eabo3153 (2022).
- D. J. Benton et al., Nature 588, 327-330 (2020).
- 5. M. Hoffmann et al., Cell 181, 271-280.e8 (2020).
- X. Xia, Viruses 13, 109 (2021).
- E. Dodero-Rojas, J. N. Onuchic, P. C. Whitford, eLife 10, e70362 (2021).
- L. V. Chernomordik, M. M. Kozlov, Nat. Struct. Mol. Biol. 15, 675-683 (2008).
- Y. Cai et al., Science 369, 1586-1592 (2020).
- 10. X. Fan, D. Cao, L. Kong, X. Zhang, Nat. Commun. 11, 3618 (2020).
- 11. W. Shi et al., Nature 619, 403-409 (2023).
- 12. Q. Huang, X. Han, J. Yan, Emerg. Microbes Infect. 11. 2412-2422 (2022).
- 13. M. A. Tortorici et al., Science 370, 950-957 (2020).
- 14. W. Li et al., Cell Rep. 38, 110210 (2022)
- 15. J. Huo et al., Cell Host Microbe 28, 497 (2020).
- 16. M. Yuan et al., Science 369, 1119-1123 (2020).
- 17. M. Lu et al., Cell Host Microbe 28, 880-891,e8 (2020).
- 18. C. O. Barnes et al., Nature 588, 682-687 (2020).
- 19. L. A. VanBlargan et al., Nat. Med. 28, 490-495 (2022).
- 20. M. Thompson et al., "Effectiveness of a third dose of mRNA vaccines against COVID-19-associated emergency department and urgent care encounters and hospitalizations among adults during periods of delta and omicron variant predominance VISION Network, 10 States, August 2021-January 2022," Morbidity and Mortality Weekly Report No. 4 (Centers for Disease Control and Prevention, 2022).
- 21 H Gruell et al. Nat. Med. 28, 477-480 (2022).
- 22. H. Zhou, B. M. Doosta, N. R. Landau, T. Tada, Viruses 14, 1334 (2022)
- 23. Y. Cao et al., Nature 608, 593-602 (2022).
- 24. K. D. McCormick, J. L. Jacobs, J. W. Mellors, Science 371, 1306-1308 (2021).
- 25. F. Muecksch et al., Immunity 54, 1853-1868.e7 (2021).
- 26. P. Shah, G. A. Canziani, E. P. Carter, I. Chaiken, Front. Immunol. 12, 637651 (2021).

- 27. P. Zhou et al., Immunity 56, 669-686,e7 (2023)
- 28. Y. Zhu, D. Yu, H. Yan, H. Chong, Y. He, J. Virol. 94, e00635-20 (2020)
- 29. S. Xia et al., Cell Res. 30, 343-355 (2020).
- 30. P. Zhou et al., Sci. Transl. Med. 14, eabi9215 (2022).
- 31. C. Dacon et al., Cell Host Microbe 31, 97-111.e12 (2023). 32. X. Sun et al., Nat. Microbiol. 7, 1063-1074 (2022).
- 33. D. Pinto et al., Science 373, 1109-1116 (2021).
- 34. K. W. Ng et al., Sci. Transl. Med. 14, eabn3715 (2022).
- 35. F. Amanat et al., Cell 184, 3936-3948.e10 (2021).
- 36. A. S. Heffron et al., PLOS Biol. 19, e3001265 (2021).
- 37. A. B. Kapingidza et al., Nat. Commun. 14, 7897 (2023). 38. W. Pang et al., Cell Res. 32, 1068-1085 (2022).
- 39. M. F. Jennewein et al., Cell Rep. 36, 109353 (2021).
- 40. N. K. Hurlburt et al., Commun. Biol. 5, 342 (2022)
- 41. T. J. Yang et al., Nat. Struct. Mol. Biol. 28, 731-739 (2021).
- 42. R. Yan et al., Science 367, 1444-1448 (2020).
- 43. E. P. Barros et al., Biophys. J. 120, 1072-1084 (2021).
- 44. B. Turoňová et al., Science 370, 203-208 (2020).
- 45. H. Yao et al., Cell 183, 730-738.e13 (2020).
- 46. Y. Song et al., Proc. Natl. Acad. Sci. U.S.A. 120, e2213332120 (2023).
- 47. L. Tai et al., Proc. Natl. Acad. Sci. U.S.A. 118, e2112703118 (2021).
- 48. C. Liu et al., Structure 28, 1218-1224.e4 (2020).
- 49. J. K. Noel et al., PLOS Comput. Biol. 12, e1004794 (2016).
- 50. W. Shi et al., Structure 30, 1233-1244.e7 (2022).
- 51. M. M. Sauer et al., Nat. Struct. Mol. Biol. 28, 478-486 (2021)
- 52. L. Casalino et al., ACS Cent. Sci. 6, 1722-1734 (2020).
- 53. J. Zou et al., Viruses 15, 1855 (2023).
- 54. C. B. Jackson, M. Farzan, B. Chen, H. Choe, Nat. Rev. Mol. Cell Biol. 23, 3-20 (2022).
- 55. Y. Huang, C. Yang, X. F. Xu, W. Xu, S. W. Liu, Acta Pharmacol. Sin 41. 1141-1149 (2020).
- 56. D. Wrapp et al., Science 367, 1260-1263 (2020).
- 57. A. C. Walls et al., Cell 183, 1735 (2020).
- 58. Q. Wang et al., Cell 181, 894-904.e9 (2020).
- 59. J. Lan et al., Nature 581, 215-220 (2020).
- 60. A. H. Wong, D. Zhou, J. M. Rini, J. Biol. Chem. 287, 36804-36813
- 61. W. A. Weihofen, J. Liu, W. Reutter, W. Saenger, H. Fan, J. Biol. Chem. 279, 43330-43335 (2004).
- 62. A. H. M. Wong et al., Nat. Commun. 8, 1735 (2017).
- 63. M. W. Grunst et al., Structure and inhibition of SARS-CoV-2 spike refolding in membranes. Dryad (2024); https://doi.org/ 10.5061/drvad.ncisxkt3h.
- 64. E. Dodero-Rojas et al., SpikeSimulations: Protocols for simulating and analyzing the SARS-CoV-2 spike protein. Zenodo (2024); https://doi.org/10.5281/zenodo.11081576.

ACKNOWLEDGMENTS

Cryo-EM data were collected at the Yale CryoEM Resource. We thank AMD for the donation of critical hardware and support resources from its HPC Fund that made this work possible. We also acknowledge generous support from the Northeastern University Discovery cluster and the Northeastern University Research Computing staff. The views expressed in this manuscript are those of the authors and do not reflect the official policy or position of the Uniformed Services University, US Army, the Department of Defense, or the US government. Funding: This work was supported by NIH grant R01 Al163395 to W.M.; NIH grant F31 Al176650 to M.W.G.; NIH grant R35GM153502-01 to P.C.W.; CIHR grant 177958 to W.M., M.P., and A.F.; a Canada Research Chair on Retroviral Entry RCHS0235 950-232424 to A.F.: the National Science Foundation (NSF) grant PHY-2210291 to J.N.O.: NSF MCB-1915843 to P.C.W.; and a grant from the Welch Foundation (Grant C-1792) to J.N.O. Work at the Center for Theoretical Biological Physics was supported by the NSF grant PHY-2019745 to J.N.O.; M.W.G. is a recipient of a Gruber Science Fellowship and was supported by NIH T32 AI055403. J.P. was supported by a CIHR Doctoral Fellowship. J.N.O. is a Cancer Prevention Research in Texas Scholar in Cancer Research, Author contributions: M.W.G., W.L., W.M., J.N.O., and P.C.W. conceived experiments. M.W.G., W.L., and S.W. acquired cryo-ET data. M.W.G., W.L., and Z.Q. analyzed cryoET data. M.W.G. performed virus-cell fusion experiments. M.W.G. and S.D. performed spike binding and neutralization experiments, F.D.-R. performed MD simulation experiments. J.P. and Y.C. generated reagents. Y.H. and X.X. generated the XBB.1.5 $_{\!\Delta 3678}.$ M.W.G., W.L., Z.Q., E.D.-R., S.D., M.P., and P.C.W. generated figures. M.W.G., W.L., and W.M. wrote the original manuscript draft. All authors reviewed and edited the manuscript. M.W.G., W.L., A.F., M.P., J.N.O., P.C.W., and W.M. supervised the work, W.M., M.W.G., A.F., M.P., J.N.O., and P.C.W. acquired funding. Competing interests: A.F. is an inventor on a provisional patent application on the CV3-25 monoclonal antibody

at The Fred Hutchinson Cancer Research Center (patent no. WO2022/140845). All other authors declare no conflicts of interest. **Data and materials availability:** The cryo-EM structures have been deposited to the Electron Microscopy Data Bank (EMDB). Cryo-ET structural maps for prefusion SARS-CoV-2 spike bound to ACE2 dimer, Prehairpin intermediate of SARS-CoV-2 spike, Postfusion SARS-CoV-2 spike, ACE2 dimer bound to one RBD, ACE2 dimer bound to two RBD, and ACE2 monomer bound to one RBD in membranes have been deposited with accession codes EMD-42857, EMD-42859, EMD-42856, EMD-42876, and EMD-42877, respectively. Data from biological assays, scripts,

and MD simulations have been deposited to Dryad (63). All force fields, structural models, simulation input decks, and analysis scripts are available for download at https://github.com/Whitford/SpikeSimulations, archived at Zenodo (64).The attenuated (BSL-2) SARS-CoV-2 del3678 is available from X.X. under a materials transfer agreement with the University of Texas Medical Branch at Galveston. License information: Copyright © 2024 the authors, some rights reserved; exclusive licensee American Association for the Advancement of Science. No claim to original US government works. https://www.science.org/about/science-licenses-journal-article-reuse

SUPPLEMENTARY MATERIALS

science.org/doi/10.1126/science.adn5658 Materials and Methods Figs. S1 to S14 Tables S1 to S3 References (65–100) Movies S1 and S2 MDAR Reproducibility Checklist

Submitted 20 December 2023; accepted 15 July 2024 10.1126/science.adn5658

Grunst et al., Science 385, 757-765 (2024) 16 August 2024 9 of 9